




# Microstructure evolution and mechanical properties of simulated HAZ in a Ni-17Mo-7Cr superalloy: effects of the welding thermal cycles

Shuangjian Chen<sup>1,\*</sup> , Li bin Zhao<sup>2</sup>, Jinjun Wang<sup>3</sup>, Chaowen Li<sup>1</sup>, Zhijun Li<sup>1</sup>, Xiang-Xi Ye<sup>1</sup>, D. K. L. Tsang<sup>1</sup>, and Kun Yu<sup>1</sup>

<sup>1</sup>Thorium Molten Salts Reactor System Center, Shanghai Institute of Applied Physics, Chinese Academy of Sciences, Shanghai 201800, People's Republic of China

<sup>2</sup>Nuclear and Radiation Safety Center, Beijing 102400, People's Republic of China

<sup>3</sup>College of Mechanical and Electrical Engineering, Nanjing University of Aeronautics and Astronautics, Nanjing 210016, People's Republic of China

Received: 21 November 2019

Accepted: 7 June 2020

Published online:

16 June 2020

© Springer Science+Business Media, LLC, part of Springer Nature 2020

## ABSTRACT

Welding thermal cycles with different peak temperatures were reproduced by a Gleeble testing machine to simulate the heat-affected zone of a Ni-17Mo-7Cr superalloy-welded joint. The effects of the thermal cycle times and peak temperatures on the microstructure and tensile properties of the thermal simulation specimens were systematically studied. The results show that no eutectic carbides are observed below 1300 °C, even when the number of thermal cycles is increased to 5. However, the eutectic reaction occurs above 1300 °C and causes a significant change in the carbide morphology because it transforms from a granular to lamellar structure. Moreover, the carbide composition transforms from (Ni, Cr)<sub>3</sub>Mo<sub>3</sub>C for the primary carbides to Ni<sub>3</sub>(Mo, Cr)<sub>3</sub>C for the lamellar carbides after the eutectic reaction. Tensile tests show that the thermal cycle has a minor effect on the tensile properties, except when the specimen underwent 5 thermal cycles with a peak temperature of 1340 °C. This is mainly due to the severe liquation reaction caused by elevated temperatures from the welding heat source, which induces cracking along the grain boundaries and results in a degradation of the tensile properties.

## Introduction

Ni-Mo-Cr alloys have been widely used in the aerospace, chemical and nuclear industries, and they constitute an important class of superalloys [1–6].

Representative Ni-17Mo-7Cr solid solution strengthened alloy (UNS N10003 alloy) developed by Oak Ridge National Laboratory was selected as a structural material for molten salt reactor in the 1960s and thorium molten salt reactor (TMSR) in the 2010s

Address correspondence to E-mail: chenshuangjian@sinap.ac.cn

[7–11]. The UNS N10003 alloy was confirmed to have good mechanical performance at elevated temperatures, good radiation resistance and oxidation resistance and excellent molten salt corrosion resistance [9, 12, 13].

Welding is an essential processing method for the construction of nuclear reactors. Nevertheless, welded joints, in particular the heat-affected zone (HAZ), are generally thought to be the weakest parts in welded components. The HAZ is a very narrow zone where the microstructure and mechanical properties change with the heat thermal cycles during the welding process [14, 15]. The strong microstructural and mechanical heterogeneities in such a microregion may result in potential risks of welded components during long-term service. However, in view of its narrow width, it is difficult to establish an essential relationship between the welding thermal cycles and overall performance in different microregions of the HAZ. A Gleeble simulator can be used to simulate the welding process and reveal the effect of thermal cycles on the microstructural evolution and mechanical properties in HAZs [16, 17]. A previous study [18] on the microstructure in the HAZ of Inconel 617 simulated by a Gleeble machine showed that continuous lamellar structures occurred along the grain boundaries at peak temperatures (PTs) in the range from 1300 to 1350 °C, resulting in a reduction in the tensile properties with increasing PT. Mohammadi [19] simulated the weld HAZ of an API X-80 pipeline steel with four PTs and two cooling rates to study its corrosion resistance in both acidic and alkaline solutions. Their results showed that the martensite-retained austenite (M–A) phase was produced at the PT of 770 °C, and the microstructure change and corrosion resistance varied with cooling rates and PTs.

For Ni-17Mo-7Cr superalloy, a substantial amount of research has been conducted on its microstructure and properties. One consensus is that  $M_6C$  is the main carbide type in the Ni-17Mo-7Cr solid solution superalloy [20, 21]. According to the research by Jiang [21],  $M_{12}C$  also appeared in the alloy as a function of the Si content, and the  $M_{12}C$  and  $M_6C$  eutectic carbides coexisted when the silicon content was less than 0.2 wt%. For the welded alloy with a Si content greater than 0.2 wt%, all precipitates before and after the post-weld heat treatment were identified as  $M_6C$

with different morphologies [22–24]. After long-term exposure from 500 to 1000 °C, the  $M_6C$  particles precipitated in the grain boundaries [20]. However, Han [25] found that the fine carbide preferentially precipitated at the grain boundaries was  $M_{12}C$ . These carbides coexisted with the preexisting  $M_6C$  and were found to be beneficial to the creep properties. In our previous work [26], the effects of thermal aging were studied on the microstructure and mechanical properties of Ni-17Mo-7Cr superalloy-welded joints, and the results showed that there was no obvious change in the grain size or tensile properties with increasing aging time from 0 to 4000 h at 650 °C. Therefore, considering the important role of carbides in the thermal history of Ni-17Mo-7Cr superalloys, it is important to investigate the microstructure changes of carbides and their effect on the mechanical properties of the HAZ in Ni-17Mo-7Cr superalloy-welded joints.

In terms of the thermal simulation work on Ni-17Mo-7Cr superalloys, the effects of PTs (1200 °C, 1300 °C and 1350 °C) on the microstructure and tensile properties were studied by Yang et al. [27]. Their results showed that the carbide morphology changed at 1300 °C and that the tensile strength sharply decreased for the alloy that experienced thermal cycling with a PT of 1350 °C. However, there are some shortcomings in their work. First, the temperature intervals were 50 °C and 100 °C in their study. The large temperature intervals may have led to important details being overlooked. Second, the HAZ was subjected to multiple thermal cycles rather than a single cycle during the welding process; this is a concern, especially for thick plates. Thus, a simulation with multiple thermal cycles is closer to the real situation than that with a single cycle. Furthermore, it is beneficial to study the microstructure evolution and mechanical properties near the fusion line in the HAZ, which experienced multiple thermal cycles (i.e., a cumulatively large heat input).

To understand the rapid changes in the microstructure and mechanical properties in the HAZ in a Ni-17Mo-7Cr superalloy, six PTs between 1260 and 1340 °C with 20 °C intervals were studied herein. Furthermore, both single- and multipass welding thermal cycles were conducted by using a Gleeble simulator. After that, the microstructure and mechanical performance of the HAZ were systematically studied.

## Materials and methods

### Materials

The Ni-17Mo-7Cr superalloy used in this work was procured from Special Steel Shares Co., LTD (China). The alloy was first melted by vacuum induction melting and then vacuum arc melting. After that, the ingots were hot rolled into sheets with a thickness of 16 mm. Finally, the sheets were solutionized at 1177 °C for 0.5 h followed by water quenching. The nominal chemical composition is listed in Table 1. The scanning electron microscopy (SEM) image (Fig. 1) shows the microstructure of the Ni-17Mo-7Cr superalloy. Chain-like primary carbides with sizes in the range from 1 to 10 μm were nearly equiaxed and present within the grains and grain boundaries.

### Thermal simulation

Previous studies on a Ni-17Mo-7Cr superalloy showed that carbides near the fusion line changed into eutectic carbides during a welding process due to elevated temperatures [28, 29]. To evaluate the influence of thermal cycles on the microstructure and mechanical properties of the superalloy after welding, thermal simulation tests with different thermal cycles and PTs were conducted on a Gleeble simulator 3500. In the present work, automatic tungsten inert gas (TIG) welding was used to weld a Ni-17Mo-7Cr superalloy plate with a thickness of 16 mm. Prior to welding, thermocouples were welded on the surface of the plate with different distances to the edge of the welding groove. The welding current was 230 A, and the welding speed, pulse frequency and gas flow rate were 100 mm/min, 2.5 Hz and 15 L/min, respectively. The loaded thermal cycle curves were acquired from the actual welding process by an OM-DAQ-USB-2401 temperature recorder.

Figure 2 presents the geometry of the thermal simulation and tensile test specimens. Note that the temperature of the whole parallel section of the thermal simulation sample was not uniform. In fact, only the middle section of the specimens reached the

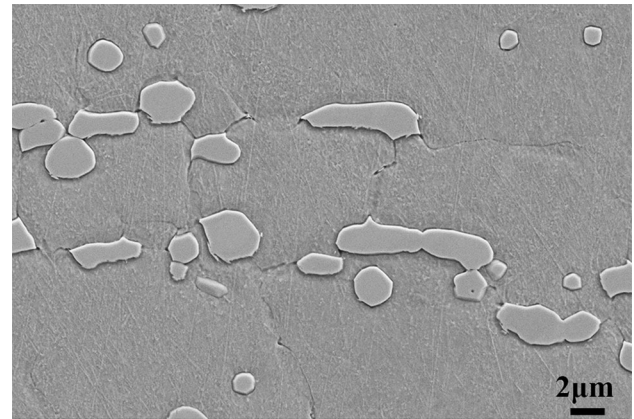


**Figure 1** Microstructure of the Ni-17Mo-7Cr superalloy, which was composed of a Ni matrix and  $M_6C$  granular carbides.

designated PT. The temperature in the rest of the specimens gradually decreased with increasing distance from the middle section.

The thermal simulation in this study was divided into two parts. The first part employed a single thermal cycle with six different PTs on the specimens to study the effect of the PT on the microstructure evolution in the Ni-17Mo-7Cr superalloy; this was conducted to determine the accurate transition temperature of the eutectic reaction for carbides in the alloy. The second part applied 5 thermal cycles with three different PTs to the specimens to simulate the microstructure changes near the fusion line in the HAZ, which actually experienced several thermal cycles (large heat input) during the welding of the thick plate. Thus, the relationship between the microstructure and mechanical properties was investigated.

The actual thermal cycle curves used in the thermal simulation tests are shown in Fig. 3. Six sets of single thermal simulation cycles were conducted at different PTs, including 1240, 1260, 1280, 1300, 1320 and 1340 °C. The heating rates in the range from 20 to 200 °C and from 200 to PT were 20 °C/s and 200 °C/s, respectively. The holding time at the PT was zero seconds. Then, the specimens were cooled in air.

To further investigate the relationship between the cumulative heat input and both the microstructure

**Table 1** Normal chemical composition of the Ni-17Mo-7Cr superalloy

Alloy	Mo	Cr	Fe	C	Si	Mn	Ni
Ni-17Mo-7Cr superalloy (wt. %)	16.5	7.0	4.0	0.06	0.3	0.5	Bal
Ni-17Mo-7Cr superalloy (at. %)	10.6	8.3	4.4	0.3	0.6	0.6	Bal

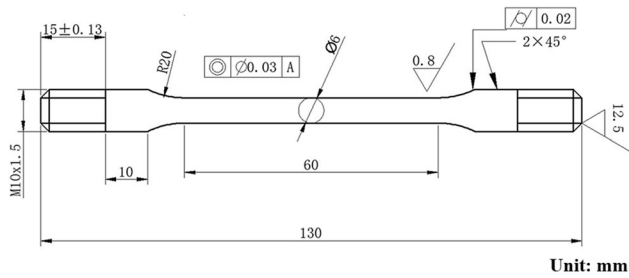
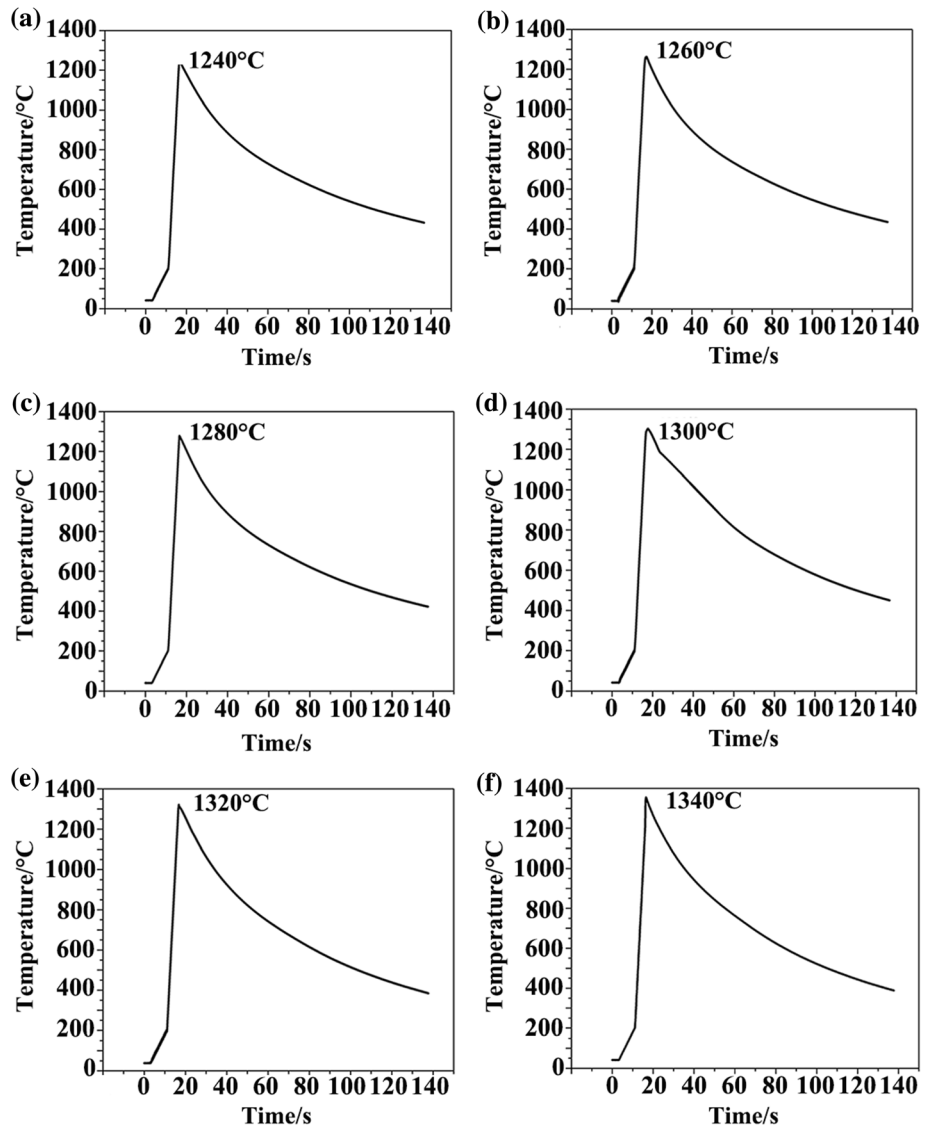


**Figure 2** Geometry of thermal simulation and tensile test specimens.

and tensile properties of the Ni-17Mo-7Cr superalloy, thermal cycles with three different PTs (1260, 1300 and 1340 °C) were loaded for five cycles in the thermal simulation tests, as shown in Fig. 4.

**Figure 3** One thermal cycles used in the thermal simulation test with different PTs:  
**a** 1240 °C, **b** 1260 °C,  
**c** 1280 °C, **d** 1300 °C,  
**e** 1320 °C, and **f** 1340 °C.

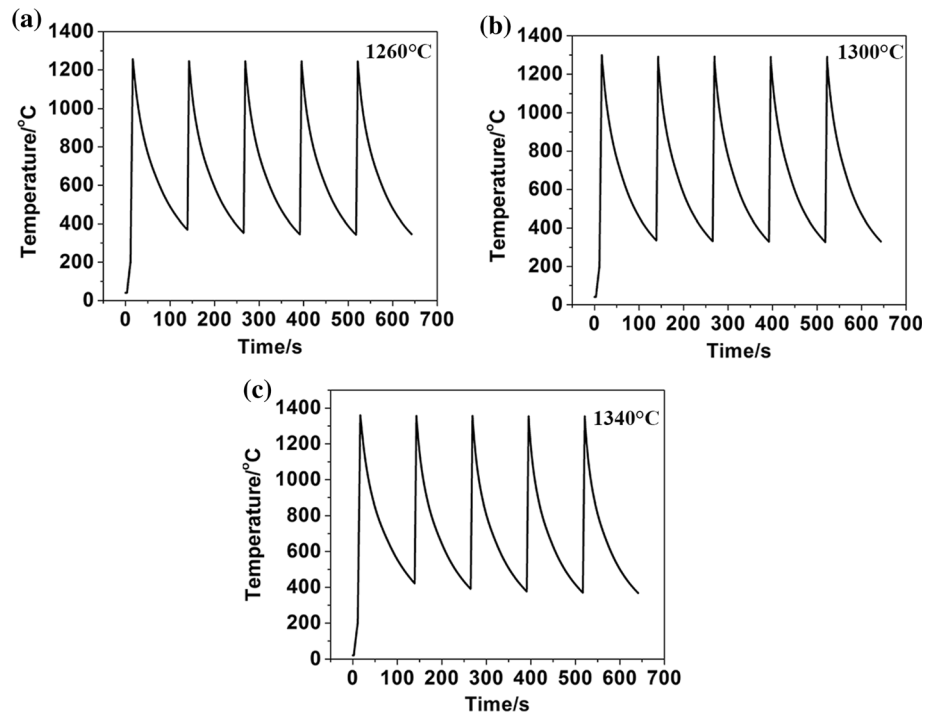


### Tensile testing and microstructure characterization

The tensile test samples were actually the same as those for the thermal simulations, as shown in Fig. 2. They were tested at 700 °C on a Zwick Z100 universal testing machine after thermal simulation. The strain rates were set as 0.005/min and 0.05/min before and after the yield point, respectively, according to ASTM E21.

Specimens for microstructural evaluation were cut from the cross sections of the thermal simulation specimens and polished with a 0.5-μm diamond paste, followed by etching with aqua regia (HCl:HNO<sub>3</sub> = 3:1) for 30 s. The microstructures of the specimens before and after tensile tests were

**Figure 4** Five thermal cycles used in the thermal simulation test with different PT values: **a** 1260 °C, **b** 1300 °C, and **c** 1340 °C.



characterized using a Zeiss LEO 1530VP scanning electron microscope equipped with energy-dispersive spectroscopy (EDS) and Oxford electron back-scattered diffraction (EBSD) systems. The measurements of the chemical compositions were taken on a SHIMADZU 1720 electron probe micro-analyzer (EPMA).

## Experimental results

### Effect of the thermal cycles on the microstructure evolution

Figures 5 and 6 show the optical micrographs and grain sizes of the thermally simulated Ni-17Mo-7Cr superalloy, respectively. These figures show that the microstructure of the thermal simulation samples varies with increasing PT. In the range from 1240 to 1300 °C, the average grain sizes are approximately 150  $\mu\text{m}$  with the exception of the grain size at 1260 °C, which is 180  $\mu\text{m}$ . When the PT exceeds 1300 °C, the grains grow as the PT increases. The grain sizes reach 177  $\mu\text{m}$  and 208  $\mu\text{m}$  at 1320 and 1340 °C, respectively. In addition, the carbide morphologies change from small particles to large chains when the PT exceeds 1300 °C.

Figure 7 shows the SEM micrographs in the center of the thermal simulation specimens after a single

thermal cycle at different PTs. With an increase in the PT from 1240 to 1280 °C, no significant change in the morphologies of carbides in the matrix is detected, as shown in Fig. 7a–c, where the morphologies are similar to that for the as-received Ni-17Mo-7Cr superalloy in Fig. 1. However, a small difference can be observed, such as the presence of thin and long tail-like carbides (indicated by the black arrows in Fig. 7) that grow from primary carbides along the grain boundaries. When the PT reaches 1300 °C, a significant change occurs in the morphology of the majority of the carbides, as shown in Fig. 7d. A large number of holes emerge in the carbides, although the carbide still retains its original shape. There is more than one type of carbide shape with multiple holes. Other carbide shapes are also observed. Long tail-like carbides grow from the original carbide and propagate along the grain boundaries, as shown in the inset of Fig. 7d. As the PT exceeds 1320 °C, a different morphology change occurs due to the complete eutectic reaction of the carbides. Two new forms, carbides with multiple holes and strip-like carbides, coexist in the alloy, as shown in Fig. 7e, f. Note that the majority of carbides are still carbides that contain multiple holes, as shown in Fig. 7e. However, at the higher PT of 1340 °C, the majority of the carbides are strip-like, as shown in Fig. 7f. Based on these results, it can be deduced that the temperature of the eutectic

**Figure 5** Optical microscopy (OM) micrographs of the thermal simulation specimens that underwent 1 thermal cycle with different PTs of **a** 1240 °C, **b** 1260 °C, **c** 1280 °C, **d** 1300 °C, **e** 1320 °C and **f** 1340 °C.

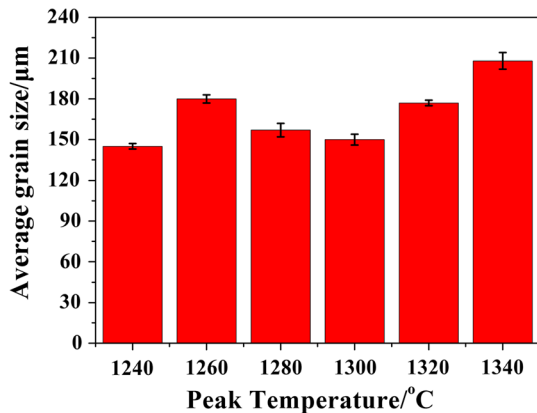
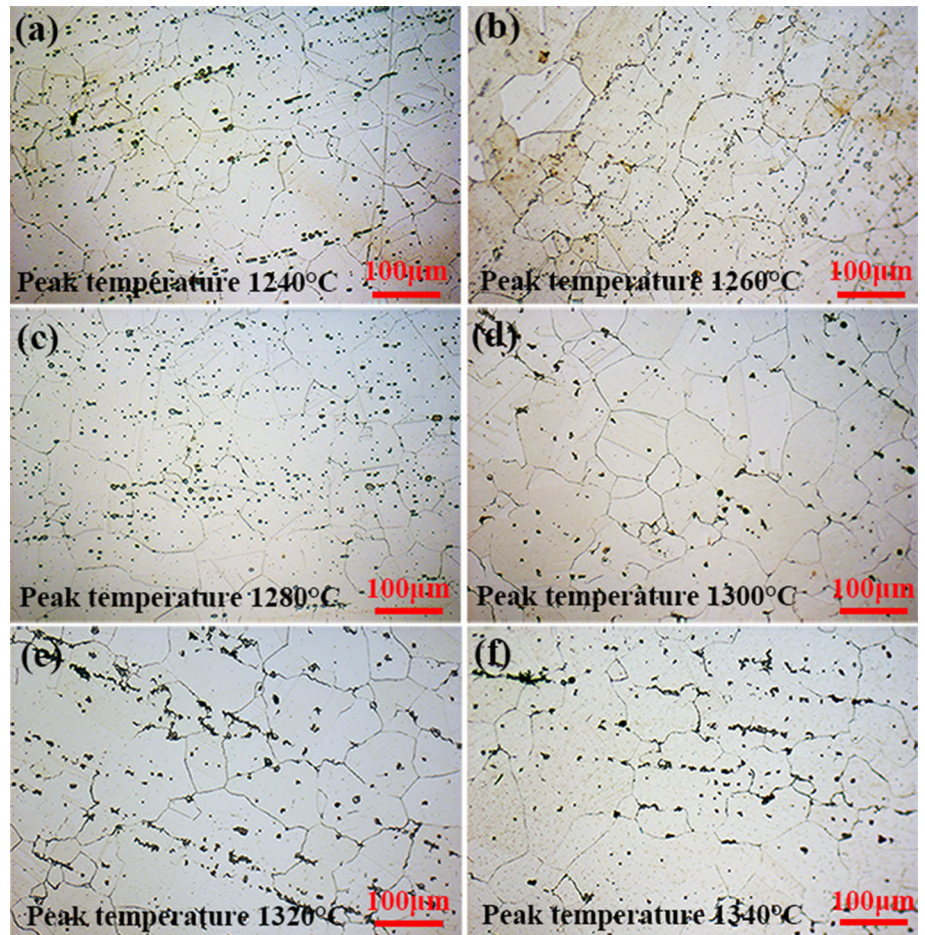


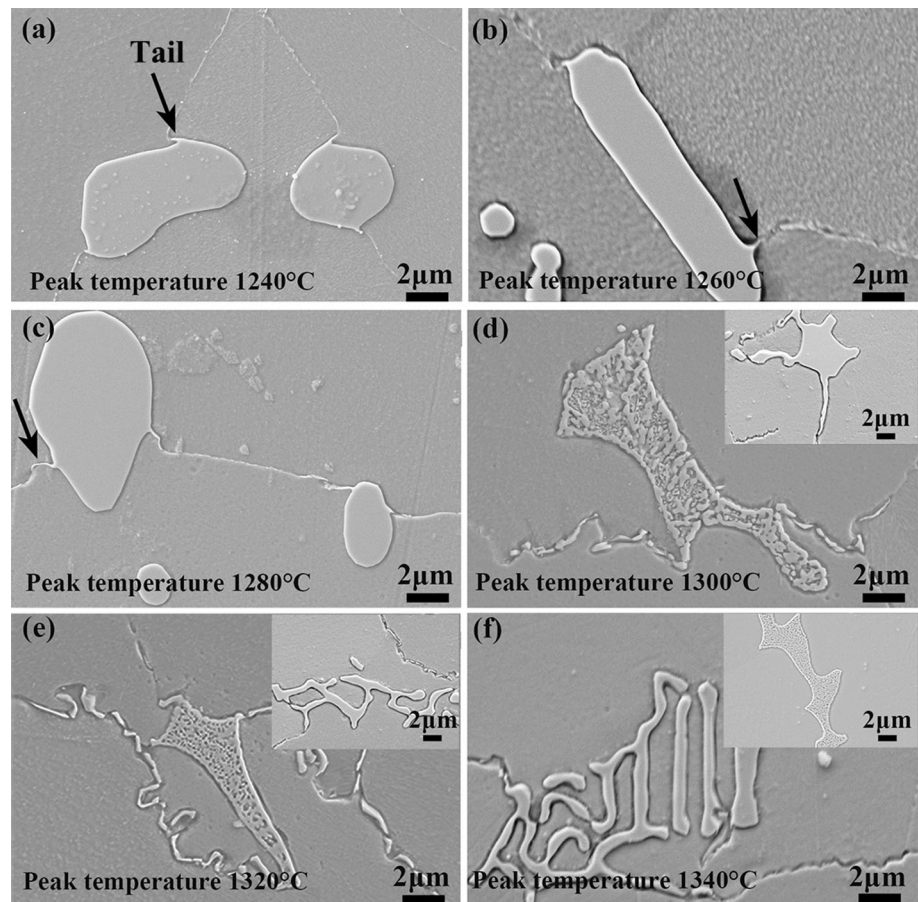
**Figure 6** Average grain sizes of the thermal simulation specimens at different PTs.

reaction starts at 1300 °C due to the significant morphology change at this temperature.

Figure 8 shows the microstructure of the specimens that underwent 5 thermal cycles. When the PT of the thermal cycle is 1260 °C, the morphologies of the matrix and carbides in Fig. 8a, b are almost the

same as that of the sample that underwent 1 thermal cycle with a PT below 1300 °C as depicted in Fig. 7a–c. However, after 5 thermal cycles with a PT of 1300 °C, the primary carbides in the samples change into a structure with multiple holes due to the eutectic reaction. It can be clearly seen in Fig. 8c, d that the dense primary carbide becomes a large number of very small particulate carbides, although its original profile is still maintained. When the PT reaches 1340 °C, the tiny particulate carbides shown in Fig. 8d cannot be detected anymore in Fig. 8e, f. It seems that the particulate carbides further grow into long strip-like carbides, and the overall morphology of the eutectic carbides becomes lamellar in appearance. The sizes of the eutectic carbides are much larger than those of the primary carbides. The length of the initial granular carbide is approximately 10 μm, while the length of the eutectic carbides can reach 30–40 μm, indicating that several primary carbides melt and combine into one large eutectic carbide after the heating process. The area indicated by

**Figure 7** SEM micrographs of thermal simulation specimens that underwent 1 thermal cycle with different PTs: **a–c** PTs of 1240 °C, 1260 °C and 1280 °C, respectively, where small tails grew from the primary carbides; **d** PT of 1300 °C, where carbides formed multiple holes; and **e, f** PTs of 1320 °C and 1340 °C, where carbides formed multiple holes and strip-like shapes after the complete eutectic reaction.



the red arrow in Fig. 8e shows that a primary carbide completely transforms into eutectic carbides.

According to a comparison of the microstructure between 1 and 5 thermal cycles, it is clear that the carbides undergo a eutectic reaction in the superalloy when the PT exceeds 1300 °C. However, when the PT is less than 1300 °C (1260 °C), the increasing heat input cannot result in a eutectic reaction, even after 5 thermal cycles. Therefore, it can be concluded that PT is a more critical factor in the eutectic reaction of carbides than the heat cycles.

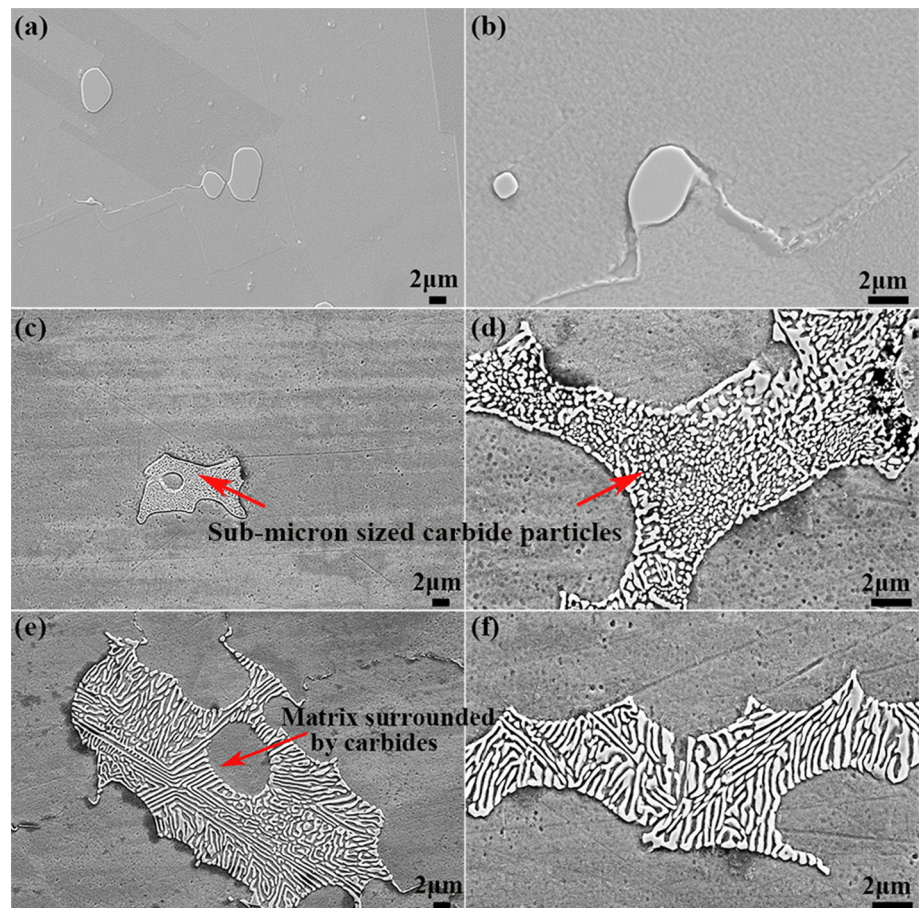
### Characterization of carbides before and after eutectic reaction

Various types of carbides may appear in nickel-based alloys, such as  $M_6C$ ,  $M_2C$ ,  $M_{12}C$  and  $M_{23}C_6$ . The  $M_6C$  tend to form when the Mo and/or W content is greater than 6–8 atomic percent [30]. For the Ni-17Mo-7Cr superalloy, the element content of Mo is more than 10 at.%. Thus,  $M_6C$  is the main type of carbides in the alloy. According to previous works

[10, 11, 21, 24, 28],  $M_6C$  and  $M_{23}C_6$  carbides have not been detected in Ni-17Mo-7Cr superalloys. However, a small amount of  $M_2C$  can form in the superalloy when the Si content is less than 0.2 wt% [21]. In addition, very small  $M_{12}C$  particles were found in the grain boundaries after long-term exposure (> 1000 h) at a high temperature of 700 °C [10, 25]. For the as-welded joint of the Ni-17Mo-7Cr superalloy with 0.27 wt.% Si, only  $M_6C$  was detected in the welded joint, including the base metal, HAZ and welded metal [24]. This finding is also supported by other studies on the characterization of carbides in Ni-17Mo-7Cr superalloys [20, 31].

The temperature in the parallel section of the sample for thermal simulation is not uniform. Only the middle part of the samples can reach the PT during the heating process. As mentioned above, the eutectic reaction is mainly affected by the temperature. There must be certain sections where fully transformed carbides, partially transformed carbides and primary carbides coexist. To further determine

**Figure 8** Microstructure after different thermal cycles was repeated 5 times with a PT of **a, b** 1260 °C, where the morphology of the carbides retains the primary shape; **c, d** 1300 °C, where the carbides completely change into a structure with multiple holes due to the eutectic reaction; and **e, f** 1340 °C, where the morphology of the carbides become lamellar.



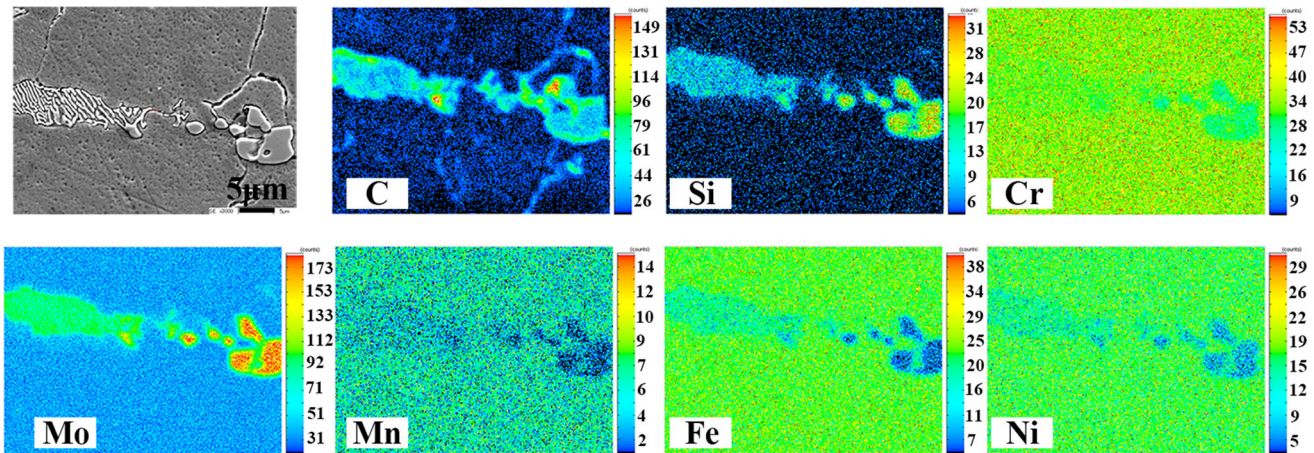
the types of carbides before and after transition, the samples are analyzed by EPMA.

Figure 9 shows a specially selected area where the whole eutectic reaction process occurs in the samples that underwent 1 thermal cycle with a PT of 1320 °C. We can see three different carbide morphologies, including fully transformed carbides, partially transformed carbides and primary carbides. In this area, the temperature is approximately 1300 °C. A fully transformed eutectic carbide is on the left side of the microstructure image in Fig. 9, while partially transformed carbides and primary carbides are on the right side. The difference in the composition of these carbides can be observed distinctly in the EPMA results. It is shown that all the carbides are rich in Mo, Si and C but lack Ni, Fe, Mn and Cr in comparison with the composition of the matrix. Moreover, the lamellar carbide lacks Mo and Si but is slightly rich in Cr, Mn, Fe and Ni in comparison with the composition of the primary carbide, which suggests that the eutectic reaction during the real welding process results in

significant variations, not only in the morphology of carbides but also in their elemental composition.

Figure 10 shows the microstructure and chemical distribution of the carbides before and after the eutectic reaction. The EDS line scan results of the primary carbides in the base metal, holey (partially melted) and lamellar eutectic carbides in the sample after 1 thermal cycle with a PT of 1320 °C are shown in Fig. 10a–c, respectively. From the EDS line scan results, the contents of Mo, Si and C in the primary carbides and holey (partially melted) carbides in Fig. 10a, b are higher than those in the matrix, while the content of Ni is much less than that in the matrix, which is consistent with the EPMA results. The zig-zag waveform curves in Fig. 10c show the same trend as that in Fig. 10a, b, in which the lamellar carbides are enriched in Mo, Si and C and lack Ni, Cr and Fe in comparison with that of the matrix. Moreover, the thermal cycles bring remarkable changes to the morphology of the carbides after the eutectic reaction. It is clear that eutectic carbides in Fig. 10c have a





**Figure 9** EPMA results of carbides before and after transition in the sample after 1 thermal cycle with a PT of 1320 °C.

lamellar structure and several parallel linear carbides grow from two long horizontal carbides.

Figure 11a shows the morphology of coexisting lamellar eutectic and partially melted carbides in the sample after 1 thermal cycle with a PT of 1320 °C. Previous studies have indicated that the primary carbides, partially melted carbides and lamellar eutectic carbides are  $M_6C$  [24], and the type of primary carbides is close to  $Ni_3Mo_3C$  [20]. EBSD is employed to further determine the crystal phase of the carbides before and after the eutectic reaction. The results show that the structures of the lamellar eutectic carbides and some partially melted carbides are both  $Ni_3Mo_3C$ , as shown in Fig. 11b, which is the same trend as that for the primary carbides.

The composition of the matrix and three kinds of carbides in the sample after 1 thermal cycle with a PT of 1320 °C are analyzed by EDS. The results are shown in Fig. 12 and Table 2. The composition of the matrix at points 1–3 is almost the same as that shown in Table 1, indicating that the EDS results are accurate and convincing. Figure 12a, b shows the primary and partially melted  $M_6C$  carbides. No significant difference in the morphology is found between them. Points 4–5 and points 6–8 in Table 2 show the corresponding compositions of the carbides. Their element contents are similar, indicating that their structure types are probably the same.

According to the EBSD result shown in Fig. 11, the lamellar and partially melted carbides are both  $Ni_3Mo_3C$ . However, it should be noted that this is not the true chemical composition, since other alloying atoms, such as Cr, could replace the Ni or Mo atoms in the  $Ni_3Mo_3C$  structure [32]. As shown in Table 2,

the (Ni + Cr): Mo ratio for the primary and partially melted carbides are 0.93:1 and 1.05:1, respectively, corroborating that both of them probably have the same carbide type and structure of  $(Ni, Cr)_3Mo_3C$ . Points 9–13 in Table 2 show the composition of lamellar carbides. The ratios of Ni:Mo and (Ni + Cr): Mo are 1.42:1 and 1.7:1, respectively, which is not consistent with the  $Ni_3Mo_3C$  structure. Since the ratio of Ni:(Mo + Cr) is close to 1:1.1, the structure of the lamellar  $M_6C$  carbides may be  $Ni_3(Mo, Cr)_3C$ , indicating that some Mo atoms are replaced by Cr atoms.

The difference in the elemental content of these three carbides implies that  $M_6C$  carbides do not have a stable chemical composition and it varies with the degree of eutectic reaction. During the eutectic reaction process, the liquid solution generates two solid phases at the same time when cooled to the eutectic temperature, while the concentration of the liquid solution depends on the time of the localized melting and element diffusion. For the lamellar carbides in Fig. 12c, the holding time above the temperature of the eutectic reaction is much longer than that of partially melted carbides in Fig. 12b. Thus, it is understandable that the composition of the partially melted carbides is slightly different from that of the primary carbides but distinctly different from that of the completely transformed eutectic carbides.

### Effect of the thermal cycles on the tensile properties of the thermal simulation specimens

The highest designed service temperature of Ni-17Mo-7Cr superalloys in TMSR is 700 °C. To study

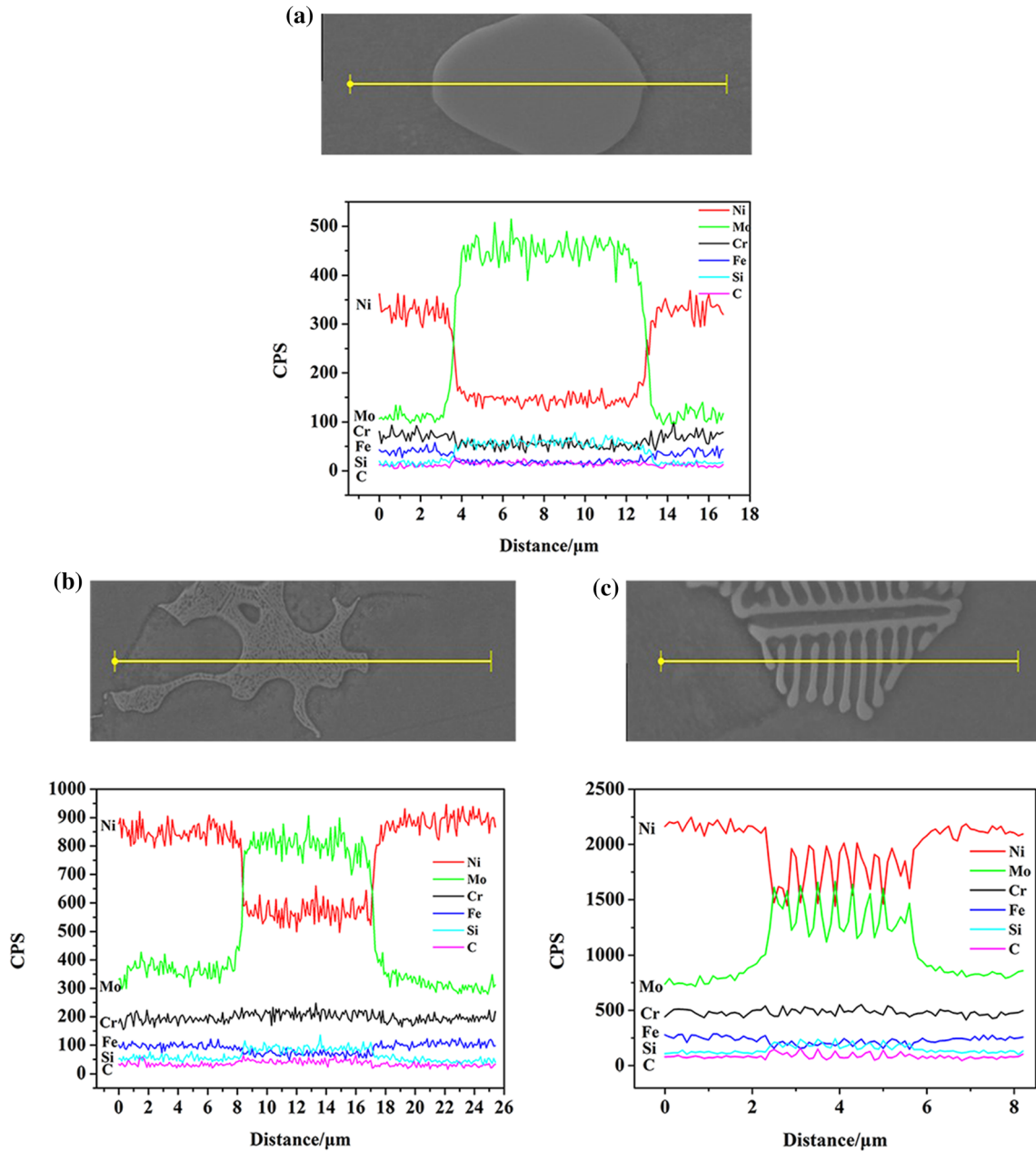


**Figure 10** EDS line scan of **a** primary carbide in the as-received alloy, **b** partially melted carbides and **c** lamellar carbides in the sample after 1 thermal cycle with a PT of 1320 °C.

the influence of welding thermal cycles on the mechanical properties, tensile tests are conducted on the thermal simulation specimens at the service temperature of 700 °C. Before the tensile tests, the thermal simulation specimens are subjected to 1 and 5 thermal cycles at different PTs (RT, 1260 °C, 1300 °C and 1340 °C).

The tensile test results for the thermal simulation specimens are shown in Fig. 13. The YS (yield

strength), UTS (ultimate tensile strength) and elongation are approximately 200 MPa, 485 MPa and 32%, respectively, indicating that the changes in the thermal cycle time and PT ( $\leq 1300$  °C) have no obvious effects on the mechanical properties. However, it is worth noting that remarkable changes in the mechanical properties occur when the PT of the thermal cycles reaches 1340 °C. For the specimen after one cycle, its mechanical properties remain

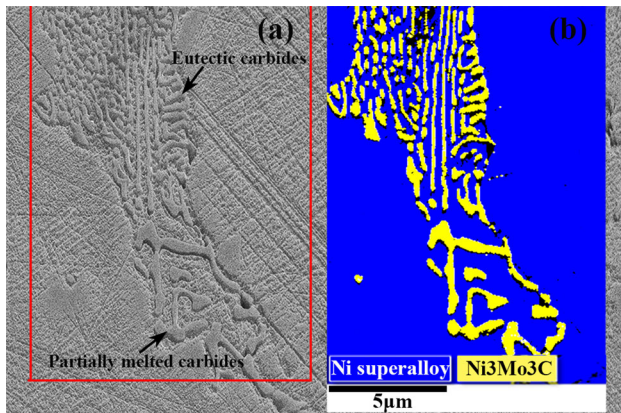
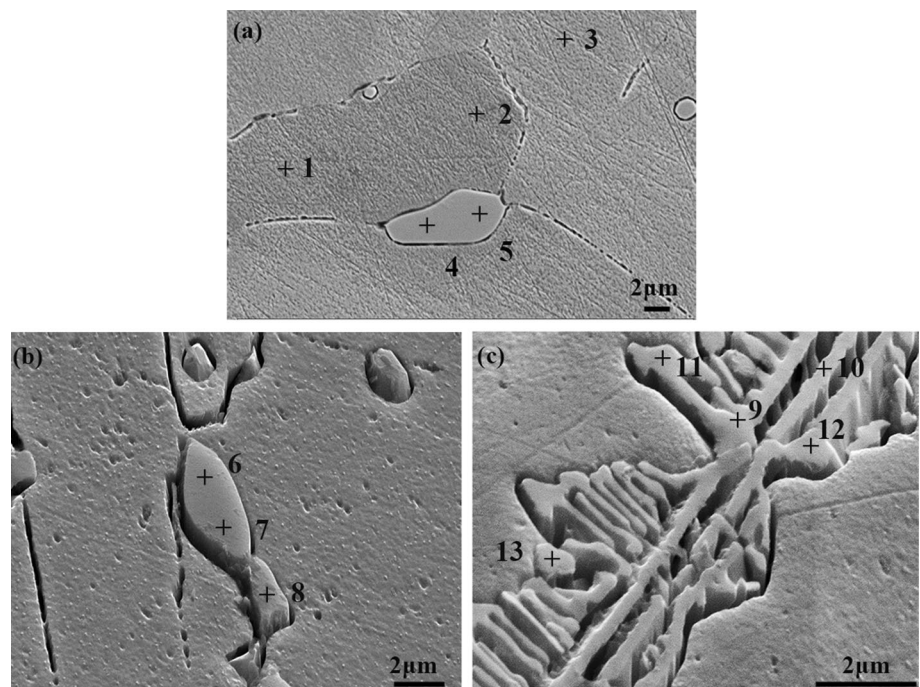


**Figure 11** **a** SEM image of the eutectic and partially melted carbides and **b** EBSD phase map in the sample after 1 thermal cycle with a PT of 1320 °C.

unchanged, and the UTS and elongation are 492 MPa and 32%, respectively. For the specimens after 5 thermal cycles, the YS remains at 200 MPa and varies slightly with the number of thermal cycles, while the UTS and elongation sharply decrease to 306 MPa and 7.1%, respectively. The deteriorated performance is mainly due to the microstructure evolution caused by the long holding time at elevated temperatures in the thermal simulation specimen, and additional details are discussed later.

**Figure 12** SEM–EDS of **a** matrix and primary carbides, **b** partially melted carbides and **c** lamellar carbides in the sample after 1 thermal cycle with a PT of 1320 °C.

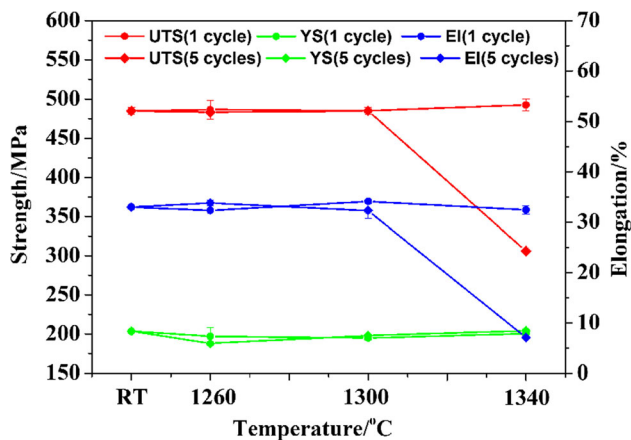


### Microstructure of thermal simulation specimens after the tensile test

The cross-sectional microstructures of the cracked thermal simulation specimens are analyzed after the tensile test. Figure 14a, b shows the microstructure near the fracture location that experiences 1 and 5 thermal cycles, respectively, with a PT of 1260 °C, and both consist of a Ni matrix and granular  $M_6C$ . No obvious differences are found between them, except that micro-cracks occur in the grain boundaries of the latter (Fig. 14b). As the PT increases to 1300 °C, significant changes in the microstructure are found, as shown in Fig. 14c, d. No carbide particles are discovered, whereas voids and eutectic carbides are simultaneously distributed along grain boundaries. The inset in Fig. 14d shows a grain almost surrounded by cracks and eutectic carbides, indicating that the bonding strength of the grain boundaries is weak and that it is easier for the specimens to fracture during the elongation process. This is mainly because eutectic carbides are able to weaken the bonding strength of grain boundaries at elevated temperatures [33]. Similar microstructures are also found in Fig. 14e, f when the PT reaches 1340 °C. The inset in Fig. 14e further confirms that the formation of voids and cracks originates from the eutectic carbides. For the specimen that experiences 5 thermal cycles, as

**Table 2** Chemical compositions of the matrix and carbides

Region	Si (at.%)	Cr (at.%)	Mn (at.%)	Fe (at.%)	Ni (at.%)	Mo (at.%)
Matrix (1–3)	1.0 ± 0.2	8.7 ± 0.2	0.7 ± 0.1	4.5 ± 0.1	74.6 ± 0.4	10.6 ± 0.1
Primary carbides (4–5)	6.8 ± 0.7	7.0 ± 0.2	0.0	1.6 ± 0.2	37.1 ± 0.7	47.6 ± 0.1
Partially melted carbides (6–8)	9.0 ± 0.8	6.3 ± 0.6	0.0	1.4 ± 0.2	39.6 ± 2.0	43.7 ± 0.8
Lamellar carbides (9–13)	6.4 ± 0.4	9.1 ± 0.2	0.6 ± 0.1	2.9 ± 0.2	47.7 ± 1.1	33.4 ± 1.0

**Figure 13** Effect of the number of thermal cycles and the PT on the tensile properties at 700 °C.

shown in Fig. 14f, long-term exposure at 1340 °C leads to tremendous changes in the microstructure. The size of the voids and width of cracks are much larger than those of other specimens. Moreover, cellular grains can be seen in the matrix.

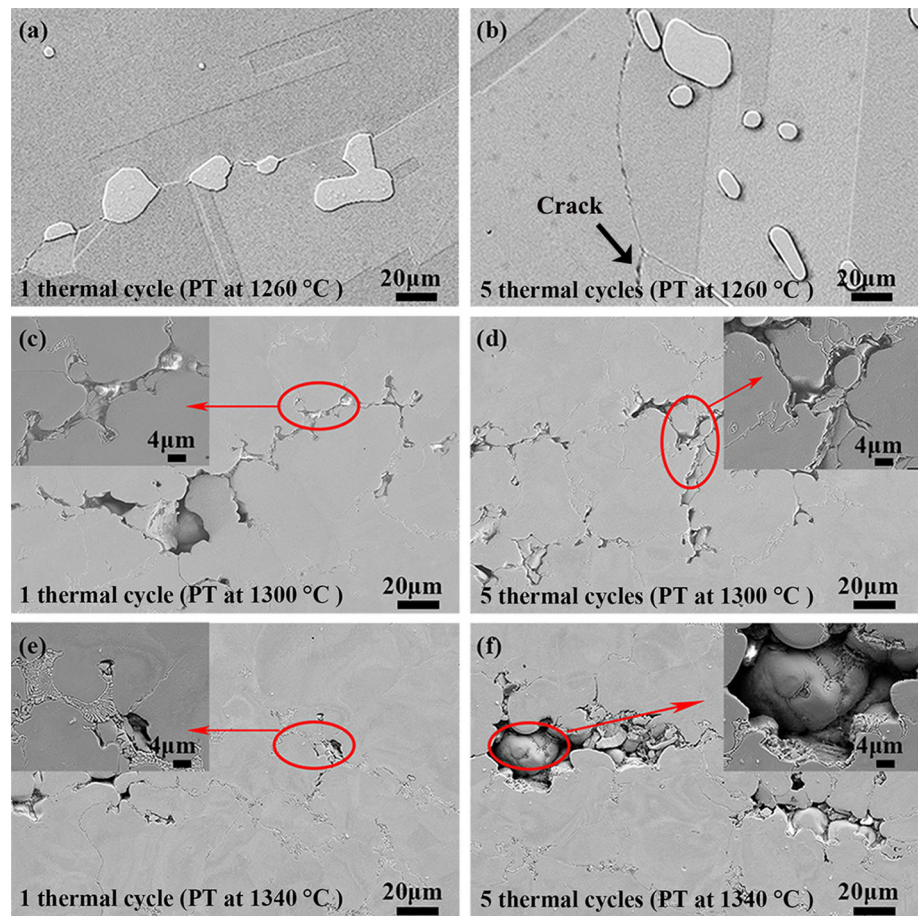
Fracture analysis is conducted on the thermal simulation specimens after tensile tests at 700 °C by SEM. The fracture morphologies are shown in Fig. 15. Figure 15a shows the specimen after 1 thermal cycle with a PT of 1260 °C. The fracture morphology shows a typical intergranular fracture feature. Note that the brittle fracture becomes very obvious after 5 thermal cycles (Fig. 15b). In addition to the intergranular characteristics, some solidification cells or dendrites distributed on the fracture surfaces result in an egg-crate-type appearance as the PT increases to 1300 °C and 1340 °C, as shown in Fig. 15c–f. The amounts of solidification cells in Fig. 15c–e seem almost the same. It is worth noting that additional solidification cells are found on the fracture surface when the specimens experience five cycles with a PT of 1340 °C. This microstructure is very loose, and distinct gaps can be clearly observed between the dendrites.

## Discussion

In this work, the effects of thermal cycling and PTs on the microstructure evolution and tensile properties of a Ni-17Mo-7Cr superalloy were studied. As mentioned above, no obvious changes in the microstructures of the alloys were observed when the PT was below 1300 °C and 5 thermal cycles. However, eutectic reaction of the primary  $M_6C$  carbides occurred when the PT was higher than 1300 °C. It was found that not only the morphologies of the carbides changed from granular primary carbides into lamellar eutectic carbides but also the types of carbides transitioned from  $(Ni, Cr)_3Mo_3C$  to  $Ni_3(Mo, Cr)_3C$ . Moreover, a large number of solidification cells and dendrites were found on the fracture surface when the PT was above 1300 °C. The smooth, rounded fracture features (Fig. 15) are normally indicative of the presence of liquid during the heating stage, showing that local melting occurred at temperatures above 1300 °C. Cracking (Fig. 14c–f) along the grain boundaries can be defined as HAZ liquation cracking, which was the direct result of localized melting.

Figure 16 shows a diagram of the microstructure evolution during the welding thermal cycling and crack initiation under a load. Figure 16a shows that the Ni-17Mo-7Cr superalloy was composed of a Ni matrix and primary  $M_6C$ . It is well known that solutes and impurity elements are not distributed uniformly in the base metal, and further segregation may occur above some critical temperature during the welding thermal cycle [30, 34]. Grain boundaries typically have a higher concentration of alloy and impurity elements, such as P, S and Si, than the alloy matrix [34, 35]. During the welding thermal cycles, some of the low solubility elements in the Ni matrix segregated aggressively to the grain boundaries, as shown in Fig. 16b. These elements are particularly harmful because they lower the solid/liquid surface energy and promote extensive wetting of the grain

**Figure 14** The cross-sectional microstructures of thermal simulation after 1 and 5 thermal cycles after the tensile test: **a, b** PT of 1260 °C, where microcracks along the grain boundaries after 5 thermal cycles can be seen; **c, d** PT of 1300 °C, where voids and cracking along the boundaries can be seen; and **e, f** PT of 1340 °C, where a large number of voids and cracking accompanied by eutectic carbides can be seen.

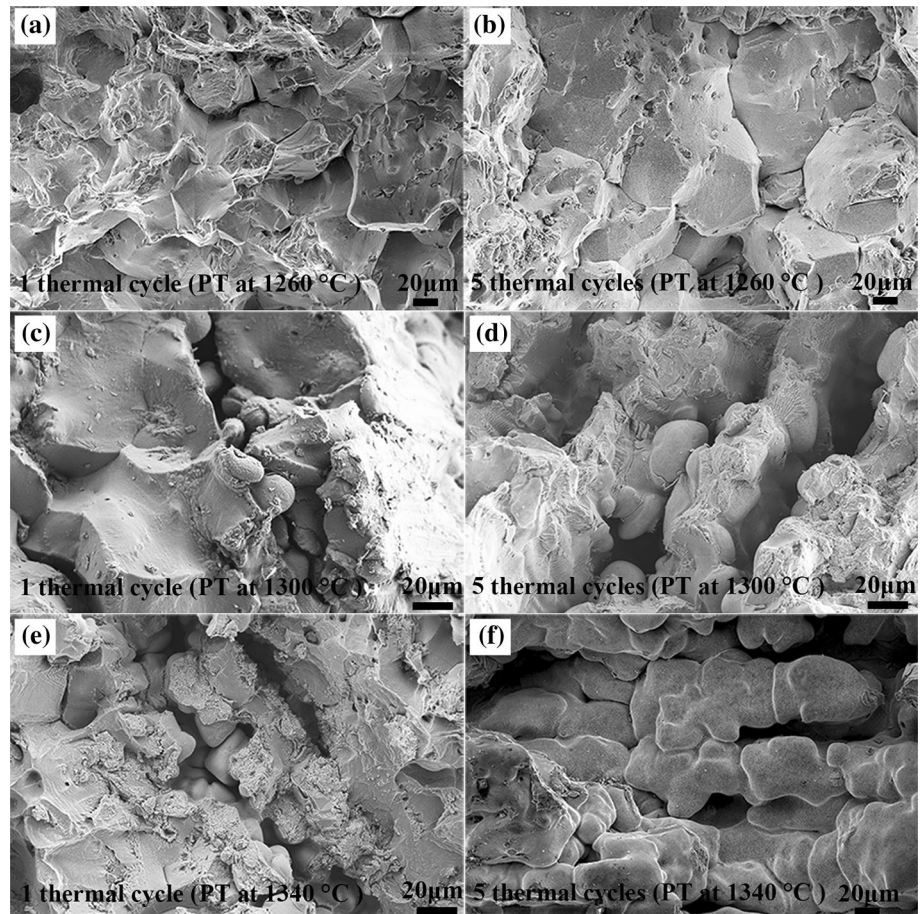


boundaries by low-melting-point compounds/films [30, 34]. When the thermal simulation specimens were subjected to thermal cycles with a PT above 1300 °C, the low-melting-point impurities locally melted (Fig. 16c). Then, during the cooling stage, the liquefied films that were distributed along the grain boundaries may have cracked due to contraction, resulting in the formation of a loose, crystalline-free cellular structure. From the cross section and fracture microstructure observations, it was noted that the morphologies and the amounts of dendrites were remarkably similar (Fig. 14c–e). This can also be seen in Fig. 15c–e, which supports the similar tensile properties of the specimens that underwent thermal cycles at 1300 °C (1 and 5 times) and 1340 °C (1 time). However, Fig. 14f and Fig. 15f show that the local melting became much worse than that of the other specimens because of the longer heat duration caused by 5 thermal cycles with a PT of 1340 °C. The local melting and loose dendrite structure severely degraded the bonding of grain boundaries and acted as

nucleation sites of cracks under an external load, as shown in Fig. 16d. Hence, the UTS and elongation of the specimens sharply decreased after 5 thermal cycles with a PT of 1340 °C, as shown in Fig. 13.

Note that the degraded mechanical properties of the specimens not only were dependent on the liquation cracking caused by local melting in the grain boundaries, as shown in Fig. 14f and Fig. 15f, but also were affected by the dispersive eutectic  $M_6C$ . The evidence is shown in Fig. 14, where the eutectic reaction occurred along the grain boundaries and in the matrix during the thermal cycles. The eutectic reaction of nickel-based alloys has been discussed in a previous work [24]; the reaction occurs during the transitory period of a thermal cycle when the temperature decreases. Since most solutes and impurities tend to diffuse and segregate along grain boundaries and interfaces between the carbides and matrix [34, 36], some metal compounds may decompose and diffuse over a short distance under rapid heating during the thermal cycles. The alloying elements,

**Figure 15** Fracture surface of thermal simulation samples after 1 and 5 thermal cycles after the tensile test: **a, b** PT of 1260 °C, where the fracture morphology with a typical intergranular fracture feature can be seen; **c, d** PT of 1300 °C, where solidification cells or dendrites are distributed on the fracture surfaces; and **e, f** PT of 1340 °C, where a large number of solidification cells and cracking can be seen on the fracture surface.

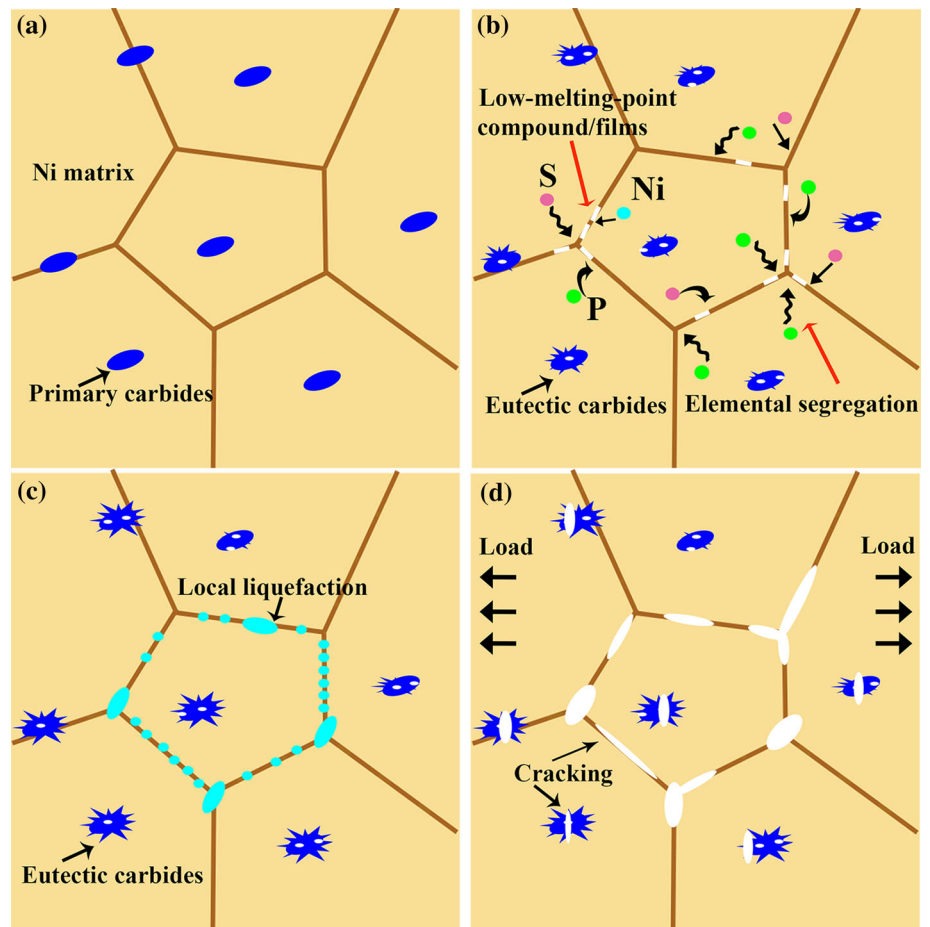


including Mo, Cr, Ni, C, S and P, enriched in the local area around the primary carbides that reach the eutectic composition point (Fig. 16b). Finally, eutectic reactions occurred, and eutectic carbides were formed (Fig. 16c). Unlike carbide particles, which can impede dislocation movement and increase grain boundary strength, these dendritic eutectic  $M_6C$  structures were very brittle and cracked under a large external strain or load, as shown in Fig. 16d.

Liquation cracking is always accompanied by cell/dendrite structures and eutectic  $M_6C$  carbides, as shown in Fig. 14 and Fig. 15. Usually, liquefaction and eutectic carbides negatively impact the mechanical properties. However, noticeable changes in the microstructure had almost no effect on the tensile properties, except for after the 5 thermal cycles at a PT of 1340 °C. This was mainly because there must be enough liquefaction area and eutectic carbides to cause crack formation during a tensile test. As mentioned above, the temperature distribution of the parallel section in the thermal simulation samples

was not uniform. Only the temperature in the middle area of the parallel section measured by thermocouples can reach the intended PT. With increasing distance from the middle section, the temperature sharply decreased. For the thermal cycle simulation with a PT of 1260 °C, Fig. 7 and Fig. 8 show that the overall microstructures were almost the same as that of the as-received alloy. Thus, it was reasonable for the UTS, YS and elongation to show little change between the thermal cycle simulation specimen with a PT of 1260 °C and the as-received alloy. Enough liquefaction area and eutectic carbides were not formed for 1 and 5 thermal cycles with a PT of 1300 °C when the eutectic reaction just occurred. Figures 5 and 8 show that after 1 and 5 thermal cycles with a PT of 1300 °C, the eutectic carbides still maintained the same profile as the primary carbides, indicating that the eutectic reaction was not sufficient and that the eutectic carbides were in the minority. For 1 thermal cycle with a PT of 1340 °C, the residence time at a high temperature over 1300 °C was

**Figure 16** Microstructure evolution during the welding thermal cycling and crack initiation **a** for the base metal, **b** during the elemental segregation and eutectic reaction of primary carbides, **c** during the local liquefaction near the grain boundaries and **d** during cracking initiation near the grain boundaries and eutectic carbides under a load.



only 1 s, which was too short to form a sufficient liquefaction area and eutectic carbides. However, the situation was completely different after 5 thermal cycles with a PT of 1340 °C, and the cumulative residence time over 1300 °C reached 5 s. The repeated heating process resulted in sufficient liquefaction and eutectic reaction. Large numbers of liquefaction areas and eutectic carbides that appeared in the simulated samples exerted obviously negative impacts on the mechanical properties. Therefore, it can be concluded from the above analysis that the high cumulative welding heat input, namely the long-term exposure at an elevated temperature, could greatly degrade the mechanical performance of Ni-17Mo-7Cr superalloys, especially in the partial HAZ near the fusion line of the welded joint. Thus, it is strongly suggested that a low welding heat input should be applied as much as possible. The interpass temperature should be controlled during welding of Ni-17Mo-7Cr superalloys.

## Conclusions

In the present work, different thermal cycles were reproduced on a Ni-17Mo-7Cr superalloy by a Gleeble 3500 machine to obtain an enlarged HAZ. The effect of thermal cycles on the microstructure and tensile properties of the simulated HAZ were systematically studied. The obtained results are summarized as follows:

- (1) The eutectic reaction caused a significant change in the morphology of the carbides when the specimen underwent thermal cycles with a PT of 1300 °C. However, the increased heat input (5 thermal cycles with a PT of 1260 °C) did not result in a eutectic reaction for the carbides.
- (2) Carbides in the Ni-17Mo-7Cr superalloy had an unstable chemical composition, which varied with the degree of eutectic reaction. The primary carbides with a  $(\text{Ni,Cr})_3\text{Mo}_3\text{C}$  structure

transformed to lamellar carbides with a  $\text{Ni}_3(\text{Mo}, \text{Cr})_3\text{C}$  structure after the eutectic reaction.

- (3) The effects of the thermal cycles (1 and 5 times) and PTs ( $\leq 1300$  °C) on the mechanical properties were negligible. However, the UTS and elongation sharply decreased when specimens underwent 5 thermal cycles with a PT of 1340 °C. This was mainly due to the liquation cracking caused by the liquefaction reaction along the grain boundaries at a high temperature and cumulative heat input.
- (4) A low welding heat input is strongly suggested for the welding of Ni-17Mo-7Cr superalloys. The interpass temperature should also be kept under a certain temperature.

## Acknowledgements

This work was supported by Shanghai Sailing Program (Grant No. 19YF1458300), National Key Research and Development Program of China (2016YFB0700404), the Natural Science Foundation of Shanghai (19ZR1468200 and 18ZR1448000), National Natural Science Foundation (Grant No. 51971238) and Youth Innovation Promotion Association, Chinese Academy of Science (Grant No. 2019264).

## Compliance with ethical standards

**Conflict of interest** No conflict of interest exists in the submission of this manuscript, and it was approved by all authors for publication.

## References

- [1] Dymek S, Wróbel M, Stepniowska E, Dollár M (2010) Microstructure stability and mechanical properties of an age-hardenable Ni–Mo–Cr alloy subjected to long-term exposure to elevated temperature. *Mater Charact* 61(8):769–777
- [2] He W, Hu R, Wu Y, Gao X, Yang J (2018) Mechanical properties of an aged Ni–Cr–Mo alloy and effect of long-range order phase on deformation behavior. *Mater Sci Eng A* 731:29–35
- [3] Zhao S, Xie X, Smith GD, Patel SJ (2003) Microstructural stability and mechanical properties of a new nickel-based superalloy. *Mater Sci Eng A* 355(1):96–105
- [4] Park NK, Kim IS, Na YS, Yeom JT (2001) Hot forging of a nickel-base superalloy. *J Mater Process Technol* 111(1):98–102
- [5] Gao Z, Wei G, Zhang C, Tan J (2017) Development of fine-grained structure in Ni–Cr–W based superalloy and its effect on the mechanical properties. *Mater Sci Eng A* 682:156–163
- [6] Ul-Hamid A, Mohammed A, Al-Jaroudi S, Tawancy H, Abbas N (2007) Evolution of oxide scale on a Ni–Mo–Cr alloy at 900 °C. *Mater Charact* 58(1):13–23
- [7] Leitnaker JM, Potter GA, Bradley DJ, Franklin JC, Laing WR (1978) The composition of eta carbide in hastelloy N after aging 10,000 h at 815°C. *Metall Trans A* 9(3):397–400
- [8] Braski DN, Leitnaker JM (1979) Homogenization of Ti–Hastelloy-N. *Metall Trans A* 10(4):427–432
- [9] McCoy HE, Gehlbach RE (1971) Influence of irradiation temperature on the creep-rupture properties of Hastelloy-N. *Nucl Technol* 11(1):45–60
- [10] Liu T, Dong JS, Wang L, Li ZJ, Zhou XT, Lou LH, Zhang J (2015) Effect of long-term thermal exposure on microstructure and stress rupture properties of GH3535 superalloy. *J Mater Sci Technol* 31(3):269–279
- [11] Han F, Zhou B, Huang H, Leng B, Lu Y, Dong J, Li Z, Zhou X (2016) The tensile behavior of GH3535 superalloy at elevated temperature. *Mater Chem Phys* 182:22–31
- [12] Wang Y, Liu H, Yu G, Hou J, Zeng C (2015) Electrochemical study of the corrosion of a Ni-based alloy GH3535 in molten (Li, Na, K)F at 700 degrees C. *J Fluor Chem* 178:14–22
- [13] Huang H, Zhou X, Li C, Jie G, Tao W, Lei G, Li J, Ye L, Huang Q, Zhu Z (2017) Temperature dependence of nickel ion irradiation damage in GH3535 alloy weld metal. *J Nucl Mater* 497:108–116
- [14] Dong XM, Wang WY, Xie JP, Xu J, Wang AQ (2011) Microstructure and fracture behaviors of welded joint of particle reinforced SiCp/ZC71 magnesium matrix composites. *Mater Sci Forum* 704–705:706–709
- [15] Silva CC, Farias JP, Miranda HC, Guimarães RF, Menezes JWA, Neto MAM (2008) Microstructural characterization of the HAZ in AISI 444 ferritic stainless steel welds. *Mater Charact* 59(5):528–533
- [16] Yue CX, Chen HD, Bai XH, Liu DS (2012) Microstructure and impact fracture behavior of simulated HAZ of F500 steel. *Trans Mater Heat Treat* 33:105–112
- [17] Li J, Li H, Peng W, Xiang T, Yang J (2019) Effect of simulated welding thermal cycles on microstructure and mechanical properties of coarse-grain heat-affected zone of high nitrogen austenitic stainless steel. *Mater Charact* 149:206–217
- [18] Liu W, Lu F, Yang R, Tang X, Cui H (2015) Gleeble simulation of the HAZ in Inconel 617 welding. *J Mater Process Technol* 225:221–228
- [19] Mohammadi F, Eliyan FF, Alfantazi A (2012) Corrosion of simulated weld HAZ of API X-80 pipeline steel. *Corros Sci* 63:323–333



- [20] Gehlbach R, McCoy H (1968) Phase instability in Hastelloy N. International Symposium on Structural Stability in Superalloys, Seven Springs Pennsylvania, pp 346–366
- [21] Jiang L, Zhang W-Z, Xu Z-F, Huang H-F, Ye X-X, Leng B, Yan L, Li Z-J, Zhou X-T (2016) M2C and M6C carbide precipitation in Ni-Mo-Cr based superalloys containing silicon. *Mater Design* 112:300–308
- [22] Wang W, Li C, Jiang L, Ye X-X, Yu K, Chen S, Li Z, Zhou X (2018) Evolution of carbide precipitates in Hastelloy N joints during welding and post weld heat treatment. *Mater Charact* 135:311–316
- [23] Yu K, Jiang Z, Leng B, Li C, Chen S, Tao W, Zhou X, Li Z (2016) Effects of post-weld heat treatment on microstructure and mechanical properties of laser welds in GH3535 superalloy. *Opt Laser Technol* 81:18–25
- [24] Chen S, Ye X-X, Yu K, Li C, Li Z, Li Z, Zhou X (2017) Microstructure and mechanical properties of UNS N10003 alloy welded joints. *Mater Sci Eng A* 682:168–177
- [25] Han F, Jiang L, Ye X, Lu Y, Li Z, Zhou X (2017) Carbides evolution in a Ni-16Mo-7Cr base Superalloy during long-term thermal exposure. *Mater* 10(5):521
- [26] Shuangjian C, Chaowen L, Kun Y, Zhijun L, Zhou X, Zhong L (2015) The effects of thermal aging on microstructural and mechanical properties of GH3535 alloy welded joint, ASME PVP Conference.
- [27] Yang J, He Y, Qin C, Zhao W, Chen S, Gao Z (2015) Microstructure evolution in a Ni-Mo-Cr superalloy subjected to simulated heat-affected zone thermal cycle with high peak temperature. *Mater Design* 86:230–236
- [28] McCoy HE, Beatty RL, Cook WH, Gehlbach RE, Kennedy CR, Koger JW, Litman AP, Sessions CE, Weir JR (1970) New developments in materials for molten-salt reactors. *Nucl Appl Technol* 8(2):156–169
- [29] He Y, Yang J, Qin C, Chen S, Gao Z (2015) Characterization of the Ni-Mo-Cr superalloy subjected to simulated heat-affected zone thermal cycle treatment. *J Alloys Compd* 643:7–16
- [30] Lippold JC (2015) *Welding Metallurgy and Weldability*. Wiley, Hoboken, New Jersey, pp 28–45
- [31] Bhattacharyya D, Davis J, Drew M, Harrison R, Edwards L (2015) Characterization of complex carbide-silicide precipitates in a Ni-Cr-Mo-Fe-Si alloy modified by welding. *Mater Charact* 105:118–128
- [32] Xu Z, Li J, Dong J, Li Z, Zhou X, Xu Z, Li J, Dong J, Li Z, Zhou X (2015) The effect of silicon on precipitation and decomposition behaviors of M6C carbide in a Ni-Mo-Cr superalloy. *J Alloys Compd* 620(620):197–203
- [33] Li J, Shrestha SL, Long Y, Li Z, Zhou X (2016) The formation of eutectic phases and hot cracks in one Ni-Mo-Cr superalloy. *Mater Design* 93:324–333
- [34] Marvel CJ, Hornbuckle BC, Darling KA, Harmer MP (2019) Intentional and unintentional elemental segregation to grain boundaries in a Ni-rich nanocrystalline alloy. *J Mater Sci* 54(4):3496–3508. <https://doi.org/10.1007/s10853-018-3056-z>
- [35] Dong J, Zhang M, Xie X, Thompson RG (2002) Interfacial segregation and cosegregation behaviour in a nickel-base alloy 718. *Mater Sci Eng A* 328(1):8–13
- [36] Furuta S, Kobayashi M, Uesugi K, Takeuchi A, Miura H, Aoba T (2017) Investigation of three-dimensional morphology changes of the eutectic Si particles affected by trace P and Sr in Al-7%Si cast alloys by means of synchrotron nano-tomography. *Mater Charact* 130:237–242

**Publisher's Note** Springer Nature remains neutral with regard to jurisdictional claims in published maps and institutional affiliations.